The Astrophysical Journal, 386:485–497, 1992 February 20

ANISOTROPIC IONIZING RADIATION IN SEYFERT GALAXIES. I. THE EXTENDED NARROW-LINE REGION IN MARKARIAN 573[1]

Zlatan Tsvetanov[2]
Department of Astronomy, University of Maryland, College Park, MD 20742

AND

J. R. Walsh
Space Telescope–European Coordinating Facility, European Southern Observatory, Karl-Schwarzschild-Strasse 2, D-8046 Garching bei München, Germany
Received 1991 July 5; accepted 1991 August 26

ABSTRACT

Narrow-band images and a grid of long-slit spectra are used to study the morphology, kinematics and ionization state of the nuclear extended narrow-line region (ENLR) of the Seyfert 2 galaxy Mrk 573. The entire ENLR is mapped spectroscopically, and velocity structure is studied. The velocity field map shows a typical galactic rotation picture with some important deviations. A simple geometric model, in accordance with the "unified schemes," is used to study effects of various parameters on the observed picture. The best match is achieved when a biconical radiation field illuminates the ISM of the host galaxy that takes part in a normal galaxy rotation but also has radial motions close to the nucleus. The emission-line images reveal a ENLR elongated along the radio axis in the northwest-southeast direction, but a map of the flux ratio $\mathscr{R}$ = [O III] λ5007/(Hα + [N II]) shows a different structure, with the highest excitation peak offset by $\sim 4''$ along the radio axis to the southeast. Several line diagnostic diagrams are produced from the grid of spectra and are used to study the ionization mechanism and angular dependence of the ionizing field. Observed line ratios are compared with photoionization models. It is shown that an accretion disk or hot blackbody ($T_{\rm BB} > 150{,}000$ K) incident spectrum produces a better fit to the line ratios than a single power-law spectrum. The general trend of the line ratios requires that the ionization parameter U initially decreases with radial distance up to approximately $2''$ (~ 1 kpc) and then increases further outward, the latter effect probably implying that the density is decreasing faster than r^{-2}. The [S II] electron density is used in conjunction with U derived from the photoionization models to estimate the angular dependence of the ionizing flux. It is shown that the number of ionizing photons is higher along the axis than in a perpendicular direction, again suggesting the presence of an anisotropic, biconical, shaped ionizing field as in the unified model of AGNs.

Subject headings: galaxies: individual (Mrk 573) — galaxies: kinematics and dynamics — galaxies: nuclei — galaxies: Seyfert

1. INTRODUCTION

One of the basic questions in studying active galactic nuclei (AGNs) is whether various observationally classified types of active galaxies are intrinsically different or whether they are different manifestations of basically the same phenomenon. Recently, there has been much speculation that differences between AGN types can be explained in terms of collimated nuclear radiation and orientation effects. This scenario has become known as the "unified scheme" (Lawrence & Elvis 1982; Lawrence 1987; Browne 1989; Orr & Browne 1982; Barthel 1989; Urry, Maraschi, & Phinney 1991). The basic idea is that radiation at optical, UV, and probably soft X-ray wavelengths is emitted anisotropically from the nucleus into two wide, oppositely directed, cones, presumably through shadowing by some sort of thick disk or torus. The major consequence is that many characteristics, such as broad line and optical/UV luminosities, depend strongly on the orientation. In particular, the line of sight is supposed to be within the opening angle of the cone in type 1 Seyfert galaxies, while Seyfert 2's are viewed "edge-on" and only extended emission regions lit up by the nucleus are visible in narrow lines.

Evidence of such anisotropy has come from different observational techniques: spectropolarimetry—revealing scattered radiation from the nucleus (cf. Antonucci & Miller 1985; Miller & Goodrich 1990), emission-line imaging—showing the elongated morphology of the extended narrow-line region (ENLR; cf. Haniff, Wilson, & Ward 1988, hereafter HWW88, Pogge 1989), and long-slit spectroscopy—indicating line ratios typical of a hard ionizing continuum (cf. Unger et al. 1987). A so-called energy deficit, in which the number of ionizing photons toward the ENLR is much higher than in the direction to Earth, is found in many cases (Kinney et al. 1991). The details of the presumed collimating disk or torus remain unknown, and different mechanisms may dominate in different type of objects (see Urry et al. 1991). For Seyfert galaxies, the most plausible explanation of the observational facts seems to be an obscuration from a thick accretion disk or torus. An obvious way to put constraints on the unification scenario is to study nearby individual objects with ENLR in detail.

Mrk 573 has been the subject of several studies in recent years. At radio wavelengths the VLA 6 cm map published by Ulvestad & Wilson (1984) reveals a triple radio source with a central component close to the optical nucleus and two lobes of similar luminosity displaced by $\sim 1\overset{''}{.}5$ along the radio axis at

[1] Based on observations collected at the European Southern Observatory, La Silla, Chile.

[2] Present address: Center for Astrophysical Sciences, The Johns Hopkins University, Baltimore, MD 21218.

PA 125°. The existence of an extended emission-line region was first reported by Unger et al. (1987) from long-slit spectroscopic observations. These authors detected high-excitation gas up to ~6″ to the NW and SE of the nucleus along the radio axis. Narrow-band [O III] λ5007 and Hα images of the object (HWW88) show an elongated emission-line nebulosity extending about 13″ and aligned to within the errors with the radio axis. Preliminary results (Tsvetanov et al. 1989) confirmed these results and also show that the maximum of the line ratio $\mathscr{R}$ = [O III] λ5007/(Hα + [N II])[3] is shifted to the SE of the nucleus. Haniff, Ward, & Wilson (1991 hereafter HWW91) published a line ratio map $\mathscr{R}$ where the distribution of the high-ionization gas suggests the presence of two oppositely directed cones of ionizing radiation. High-resolution spectroscopy by Whittle et al. (1988) reveals components in the [O III] λ5007 line profile associated with the ratio lobes. The central part shows essentially solid-body rotation, but velocity displacements of [O III] λ5007 components suggest a possible outflow in addition to the normal galaxy rotation. This is in good agreement with preliminary analysis of our spectroscopic data (Tsvetanov 1989).

Mrk 573 was observed in detail as part of a program to study the anisotropic radiation field in Seyfert galaxies. In this paper we present the entire observational material as well as a detailed discussion of velocity and ionization pattern of the extended NLR. All distances are calculated assuming $H_0 = 75$ km s^{-1} Mpc^{-1}. The results are interpreted in the framework of the "unified schemes."

2. OBSERVATIONS AND REDUCTIONS

The observations of Mrk 573 were taken with the ESO Faint Object Spectrograph and Camera (EFOSC) on the ESO 3.6 m telescope at La Silla, Chile (Melnick et al. 1989). An RCA CCD (type SID 503) in 2 × 2 binned mode was used as detector. This led to relatively big pixels (0″.675), which compares with the estimated seeing of 1″.3. Images through interference filters (typical Δλ ~ 60 Å), centered on the redshifted wavelengths of [O III] λ5007, Hα and the [S II] λλ6716, 6731 doublet (on-line) and on continuum regions adjacent to [O III] λ5007 and Hα (off-line), were obtained. Two relatively short exposure frames were taken in each filter in order not to saturate the nucleus and to clean cosmic-ray events afterwards. In this approach, the outer faint parts of the galaxy disk are lost, but the S/N ratio in the circumnuclear region is high enough for the purposes of this study. The log of the observations is presented in Table 1.

Two types of spectroscopic observations were taken with the same instrumentation in single-slit mode (pixel size along the slit: 0″.675). Low-resolution spectra using B300 and R300 grisms were taken through the nucleus at PA 270° to cover the wavelength region from below 3600 Å to almost 1 μm in two steps with inverse dispersion of ~7 Å pixel^{-1} and ~8.5 Å pixel^{-1}, respectively. In addition a grid of medium-resolution spectra was taken with the O150 grism which gives a scale of 3.8 Å pixel^{-1} along the dispersion and a spectral range of 5050–7000 Å. This grid was taken by offsetting the telescope perpendicular to the slit in steps of 1″.5. The slit was 1″.5 wide, and the grid covers almost the entire nuclear extended emission-line region. To check the offset of the telescope, snapshot images were taken after each slit position. Thus the real

TABLE 1

OBSERVING LOG

Date (1988)	Seeing	Exposure (s)	Dispersion (Å pixel^{-1} or filter's $\lambda_c/\Delta\lambda$ Å)	Comments
		Spectra		
Aug 6........	1.3	600	6.8	3600–6800 Å, PA 270°
		600	8.5	6000–9800 Å, PA 270°
		6 × 300	3.8	Grid of six slit positions 5050–7000 Å, PA 270°
		Images		
Aug 9........	1.3	2 × 180	5111/55	[O III] λ5007 on-line
		2 × 180	5211/55	[O III]λ5007 off-line
		2 × 180	6693/94	Hα on-line
		2 × 180	6766/68	Hα off-line
		2 × 180	6832/74	[S II] λλ6716, 6731

offsets are estimated to have an accuracy of 0″.1 from the positions of a few stars in the field.

The images were processed with the MIDAS software package. Bias and dark subtraction and flat-fielding were performed in the usual way. Further reduction followed the procedure decribed in detail by di Serego Alghieri (1987, 1990). There are several stars in the field which were used to align the images by means of fitting Gaussians to stellar images. The alignment accuracy, as estimated by comparing offsets derived from different stars, is better than 0.1 pixel. At this point, a pair of images in each filter were averaged using the kappa-sigma algorithm to eliminate cosmic-ray signatures (see MIDAS manual for details). Following the alignment, the continuum images were scaled to the line + continuum ones assuming that the spectrum of the underlying galaxy is similar to the spectrum of the "standard" elliptical galaxy (Yee & Oke 1978) over the range covered by the filters. This assumption was later checked using our spectral data and also from the statistics of the residuals after subtraction of the galaxy; the flux-scaling factors were thus estimated to have an error of less than 5%. The images were flux-calibrated using the observations of a standard star through the same filters.

The spectral observations were reduced using both the MIDAS and IRAF packages. It is important to note that part of the data originally processed with MIDAS was afterwards rereduced with IRAF, and the results (line positions and fluxes) were found to agree to within the statistical errors. Wavelength calibration was done by fitting a two-dimensional polynomial to the positions of lines in the arc frames taken before and after the grid of spectra. To account for the atmospheric dispersion and possible residual tilt of the CCD, a low-order polynomial was fitted to the position of the continuum of the source assuming it is spatially unresolved. The two polynomials were included in rebinning to a linear wavelength scale. The overall accuracy of the geometric corrections, as checked from the positions of night sky lines and continuum, is of order of 0.1–0.2 pixel rms in both directions. Finally, all frames were calibrated by means of standard stars (different for the low- and medium-resolution spectra) observed before the object.

Further analysis of the spectra included fitting Gaussians to the emission lines at each spatial increment along the slit. In each case the fit was judged by eye, and the procedure was stopped when the peak line flux dropped to approxmately 2–3

[3] The filter used includes lines Hα and [N II] λλ6548, 6583.

σ above the local continuum. Both the velocities of the lines were measured from the fitted Gaussians. The fact that lines cover several pixels makes it possible to determine the peak of Gaussians with an accuracy of a fraction of a pixel. The estimated velocity error ranges from ~ 30 km s^{-1} for the brightest lines up to ≥ 60 km s^{-1} for the weakest cases. On the other hand, since the dispersion was relatively low (instrumental resolution ~ 300 km s^{-1}), and the lines are only marginally broader than this instrumental profile, no velocity information is present in the profile shape. No significant difference was found between the velocities derived from different lines. Since [O III] $\lambda 5007$ is the brightest line in the observed spectral region and has the largest spatial extent, the velocity field was derived from measurements of its wavelength. The absolute flux calibration accuracy has most probably a value of $\leq 20\%$, since the night was photometric. The accuracy of the relative line intensities, however, varies with the strength of the line and is less than 10% for the brightest lines or those close to the nucleus and much worse for the weakest cases or those at the edges of the emission-line region. This was checked by comparing line ratios at the same position from both images and spectra. The results were satisfactory given the difficulties of extracting exactly the same region and the fact that [N II] $\lambda\lambda 6548$, 6583 lines were included in the Hα filter.

3. RESULTS

3.1. *Images*

The continuum-subtracted emission line images in [O III] $\lambda 5007$, Hα + [N II] $\lambda\lambda 6548$, 6583 and [S II] $\lambda\lambda 6716$, 6731 are presented in Figure 1. These basically confirm previous results, i.e., that the nuclear emission-line region is extended approximately $10'' \times 15''$ with major axis in PA 125° coinciding with the orientation of the radio axis (cf. HWW88). We have fitted ellipses to the isophotes of the line images in order to estimate the orientation more precisely. The inner part of the [O III] $\lambda 5007$ image is elongated in PA 118°, and there is a small, but noticeable, rotation of the major axis, so the outermost isophotes are elongated in PA 125°. The twist in the Hα image is even more profound running from PA 116° in the inner part to almost PA 130° at the outer edge. The errors of determining these positions are typically 3°–4°. These orientations are close to the position of the radio axis at PA 124° $\pm$ 3° (Ulvestad & Wilson 1984). Given the uncertainties in orientation and differ-

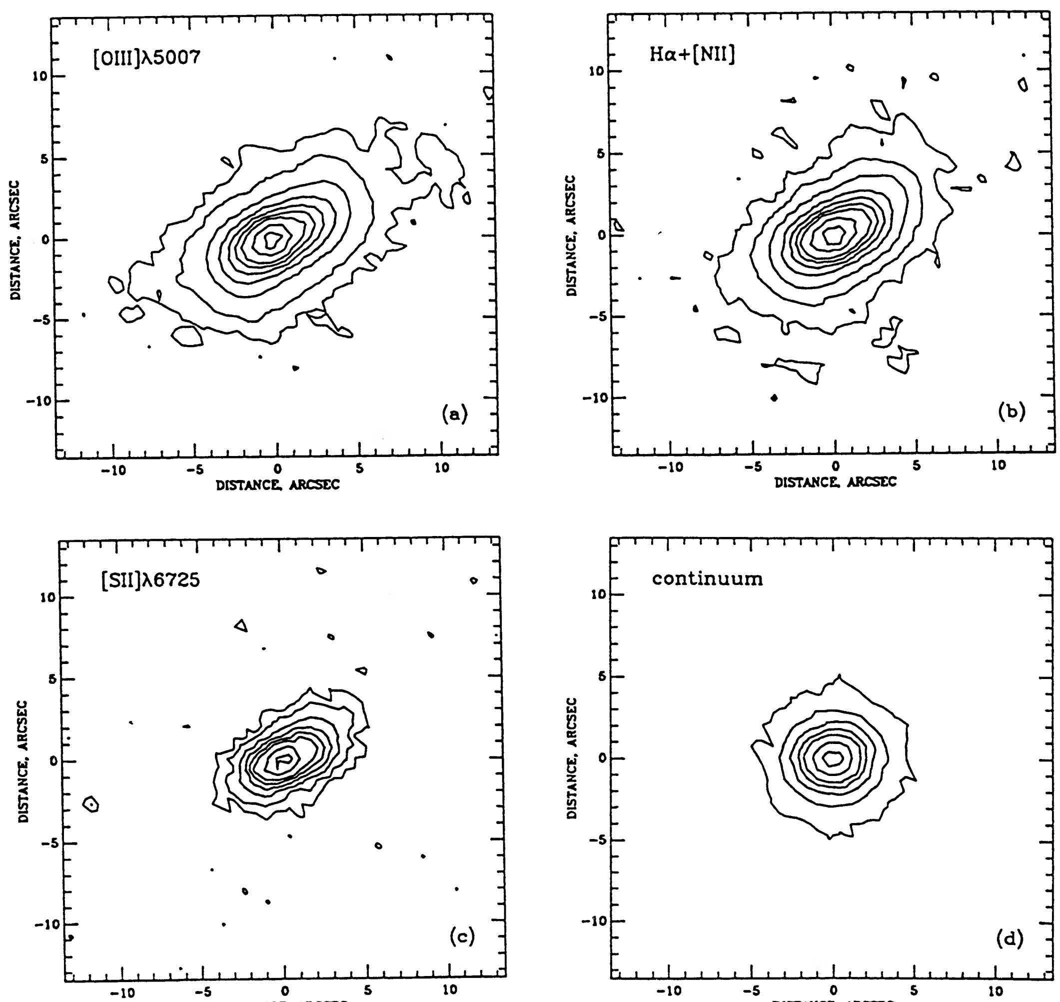

FIG. 1.—Continuum-subtracted narrow-band images of Mrk 573. (*a*) [O III] $\lambda 5007$; (*b*) Hα; (*c*) [S II] $\lambda\lambda 6716$, 6731; (*d*) continuum near [O III] $\lambda 5007$. First two contours are at 3 and 9 σ above the background and next are at 10, 20, 30, 40, 50, 70, and 90% of the peak value.

ent resolution, we conclude the ENLR is elongated along the radio axis in PA 125°, which is similar to what HWW88 have found from their images. The ellipticity of the isophotes does not change much and has an average value of $\epsilon = 0.46$ ($a/b = 1.85$). It should be noted, however, that somewhat larger a/b of the HWW88 images is probably consistent with our measurements since seeing/sampling effects will tend to make our images rounder. The continuum image on the same scale as the emission-line images has its major axis oriented roughly at PA 100°. To get an idea of the orientation at larger scale, we have analysed a digitized image of Mrk 573 obtained using the Guide Star Astrometric Package (GASP) developed at the Space Telescope Science Institute[4]. On a scale up to $\sim 20''$ from the nucleus, this image is elongated roughly north-south with an ellipticity of $\epsilon = 0.15$. At larger distances, the object is surrounded by a low surface brightness "fuzz" which is oriented in PA 70° ± 25° with an ellipticity only marginally greater than 0.

The peaks in both Hα + [N II] and [S II] filters coincide with the position of the nucleus as determined from the continuum images, but there is a small shift of the [O III] λ5007 maximum along the radio axis to the SE. This result is in accordance with Whittle et al. (1988) who notice a possible shift in the [O III] λ5007 intensity from the stellar nucleus based on high-resolution spectroscopic data. Otherwise, the surface brightness in all lines decreases smoothly outward with no visible spatial structure.

The line ratio $\mathscr{R}$ = [O III] λ5007/(Hα + [N II]) map shows a different structure (Fig. 2). A wide valley of decreased $\mathscr{R}$ passes through the nucleus in PA ~ 40°, approximately perpendicular to the elongation direction of the line images, and the maximum of the ratio $\mathscr{R}$ is significantly shifted along the radio axis from the nucleus to the SE by $\sim 4''$. A second less noticeable peak is present to the NW of the nucleus, but it is close to the edge of the image where the S/N ratio is poor.

Another important piece of information is the total line flux from the ENLR (actually nucleus plus ENLR). from our flux-calibrated images we obtain $F_{\rm tot}$([O III] λ5007) = $(15.7 \pm 0.5) \times 10^{-13}$ ergs cm^{-2} s^{-1}, $F_{\rm tot}$(Hα + [N II]) = $(9.9 \pm 0.8) \times 10^{-13}$ ergs cm^{-2} s^{-1}, and $F_{\rm tot}$([S II] λ6725) = $(2.3 \pm 0.2) \times 10^{-13}$ ergs cm^{-2} s^{-2}. The errors are determined from the statistics of the continuum-subtracted images and do not include errors associated with the flux calibration itself. The $2''.7 \times 4''$ aperture fluxes from the images are consistent to within 15% with the absolute spectrophotometry of Koski (1978).

3.2. *Velocities*

As mentioned already, velocities were measured by means of Gaussian fits to the emission lines. This provides us with a medium-resolution velocity map covering most of the ENLR and at some points extends even beyond the narrow band image. The velocity data cube is used to describe the gas motions around the Seyfert nucleus. First, the systemic velocity has been calculated by averaging all measurements, but excluding a small region around the nucleus, which is most probably affected by the activity of the central source. The heliocentric value is 5161 km s^{-1} and agrees very well with the value of 5155 km s^{-1} derived by Whittle et al. (1988) from their high-resolution spectroscopy.

[4] STScI is operated by the Association of Universities for Research in Astronomy, Inc., for NASA.

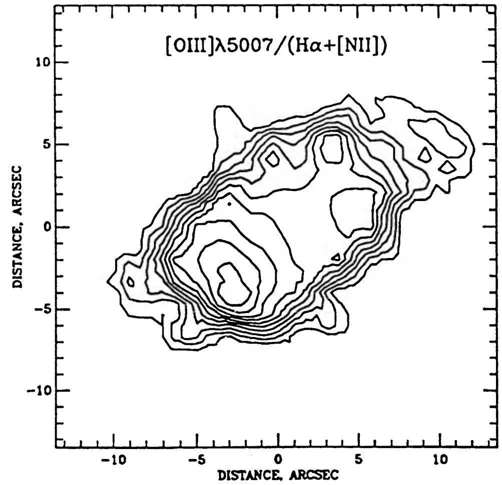

FIG. 2.—Excitation map (line ratio $\mathscr{R}$ = [O III] λ5007/(Hα + [N II]) of Mrk 573. Contours start at 0.25 and go with a step of 0.25.

Figure 3 presents the velocity map projected onto the [O III] λ5007 image. There are several important features seen on this map. There is a well-defined axis of symmetry approximately along PA 130°. The error of determining this position angle is about 5°–7° due to our poor sampling of the velocity map, but in general it is aligned to within the errors with the radio axis. On the NE side of this axis, all measurements are blueshifted with respect to the systemic velocity $V_{\rm sys}$, while on the SW side all points are redshifted. This axis presumably presents the projected rotation axis of the circumnuclear gas. At the position of the nucleus, however, the velocity is significantly blueshifted with respect to $V_{\rm sys}$ by more than 100 km s^{-1}. This is in agreement with the general trend for the nuclear velocities in active galaxies to be blueshifted with respect to the systemic velocity of the host galaxy (cf. Wilson & Heckman 1985 and references therein) and favors the presence of a radial outflow component in the gas motion.

The shape of the velocity curve at various position angles, apart from near the nucleus, is close to solid body rotation. This result is in agreement with the conclusion of Whittle et al. (1988).

3.3. *Line Intensities*

The spectral region covered by the grid of slit positions includes several important diagnostic lines, namely [O III] λ5007, [O I] λλ6548, 6583, and [S II] λλ6716, 6731. The Hα + [N II] blend and the [S II] doublet are resolved (although the lines are not fully separated) at this dispersion which allows the components to be deblended. The widths of the individual Gaussians for the [N II] and [S II] lines were forced to be equal and all other parameters were left free.

Line intensity ratios plotted versus radial distance from the nucleus are shown in Figure 4. The coordinates x, y of each pixel are calculated from the position of a given slit and from the spatial scale along the slit. There are several important features seen in this figure. Line ratios [N II] λ6583/Hα and [S II] λ6725/Hα which are inversely proportional to the ionization parameter in the range $10^{-4} < U < 10^{-1}$, increase with distance up to approximately $2''$ and then decrease further outward. Although less clear, the ratios [O I] λ6300/Hα and [O I] λ6300/[O III] λ5007 show the same behavior. There is much scatter in the [O III] λ5007/Hα panel, but the general

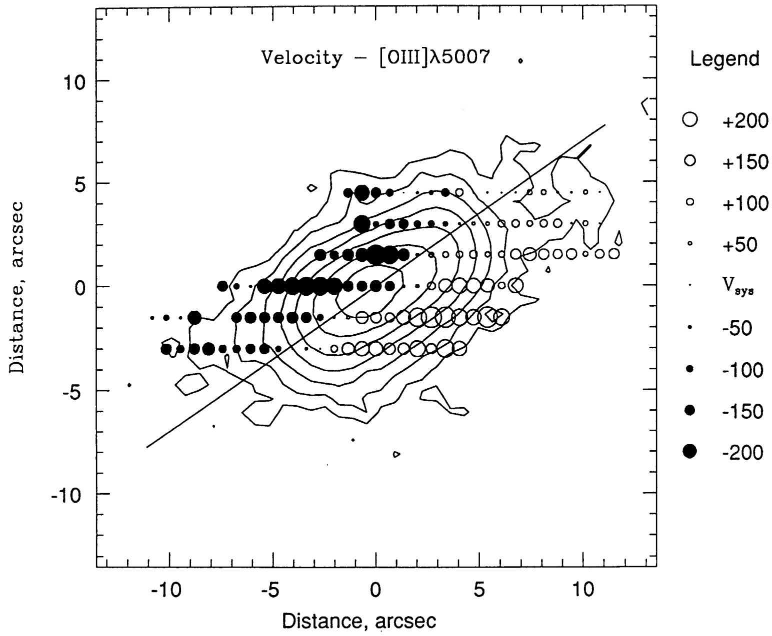

FIG. 3.—Velocity map of Mrk 573 projected onto a [O III] $\lambda 5007$ image. Filled circles are blueshifted with respect to systemic velocity and open circles are redshifted. The size of the symbols is proportional to the deviation from $V_{sys} = 5161$ km s^{-1}. The axis of symmetry in PA 125° is also shown.

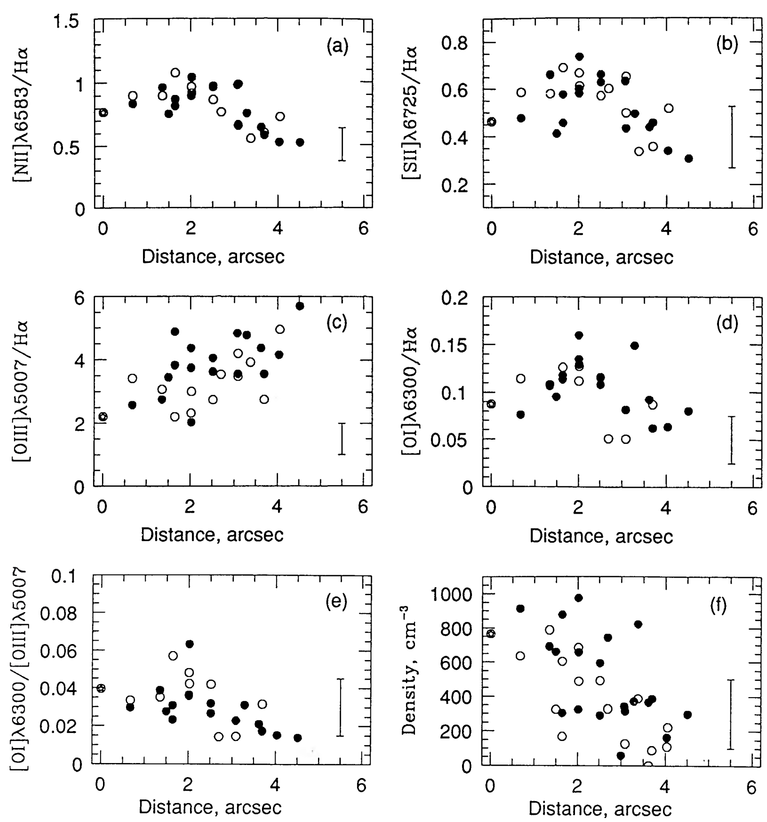

FIG. 4.—Line ratios plotted vs. radial distance from the nucleus. Open circles correspond to the NE part of the ENLR, and filled circles, to the SW part. Typical error bars are shown in the lower right hand corner of each panel.

trend is for this ratio to increase outward. The density, as estimated from the [S II] λ6716/λ6731 density sensitive ratio (see § 5.2), decreases outward especially beyond 2″ from the nucleus. This is in general agreement with the behavior of other line ratios as discussed in the next section.

Line ratio changes along the major axis of the ENLR at PA 125° (also the radio axis) are presented in Figure 5, where filled and open symbols correspond to the SE and NW side of the nucleus respectively. Line ratios [N II] λ6583/Hα and [S II] λ6725/Hα and to a lesser extent [O I] λ6300/[O III] λ5007 show two peaks some 2″ on each side of the nucleus. These are obviously related to the radio lobe positions—approximately 1″.5 away from the nucleus in the same directions (Ulvestad & Wilson 1984). These peaks in the optical line ratios seem to be slightly further away from the nucleus than the radio lobes, but the difference is only marginal given the optical spatial resolution. The [O III] λ5007/Hα ratio shows a strong peak at ~4″ SE, which coincides with the peak in the excitation map derived from the images, and also a couple of smaller peaks on the NW side. The density stays roungly constant out to ~2″ and then decreases quickly farther out.

The dependence of the line ratios on position angle with respect to the nucleus is of particular interest since it may provide an idea of the angular distribution of the ionizing radiation. In Figure 6 we present a plot of the [N II] λ6583/Hα ratio as a function of position angle. Two well-defined minima roughly at PA 125° and PA 325° are clearly seen in this figure. In a simple photoionization picture, the [N II] λ6583/Hα ratio is inversely proportional to the ionization parameter, so these two minima are reminicent of increased ionizing flux along the radio/ENLR axis. However, several other effects, such as abundance gradients, projection effects, etc., may also play a role in defining the trends seen in this diagram.

3.4. *Summary of the Results*

Below we summarize the major observational results to be used later on in modeling both the velocity and ionization patterns.

1. The emission-line region is elongated approximately 10″ × 15″ (projected axial ratio of ~1.85) and is oriented at PA 125°. This direction coincides to within the errors with the radio axis but is significantly misaligned with respect to the apparent major axis of the underlying galaxy.

2. The excitation map, line ratio $\mathscr{R}$ = [O III] λ5007/(Hα + [N II]), shows an arclike maximum ~4″ SE of the nucleus along the radio axis. A wide valley of reduced $\mathscr{R}$ passes through the nucleus roughly perpendicular to the main axis.

3. The velocity field of the ENLR is typical of rotation, with the NE part blueshifted and the SW part redshifted with respect to the heliocentric systemic velocity of V_{sys} = 5161 km s^{-1}. The projected rotation axis of the gas is aligned to within the errors with the radio axis.

4. The shape of the rotation curve in various position angles, apart from near the nucleus, is close to solid body rotation. At the position of the nucleus, the emission line velocity is significantly blueshifted with respect to systemic velocity by more than 100 km s^{-1}.

5. Line ratios which are sensitive to the ionizing parameter U indicate that the excitation decreases outward up to a distance of about 2″ and then increases further outwards.

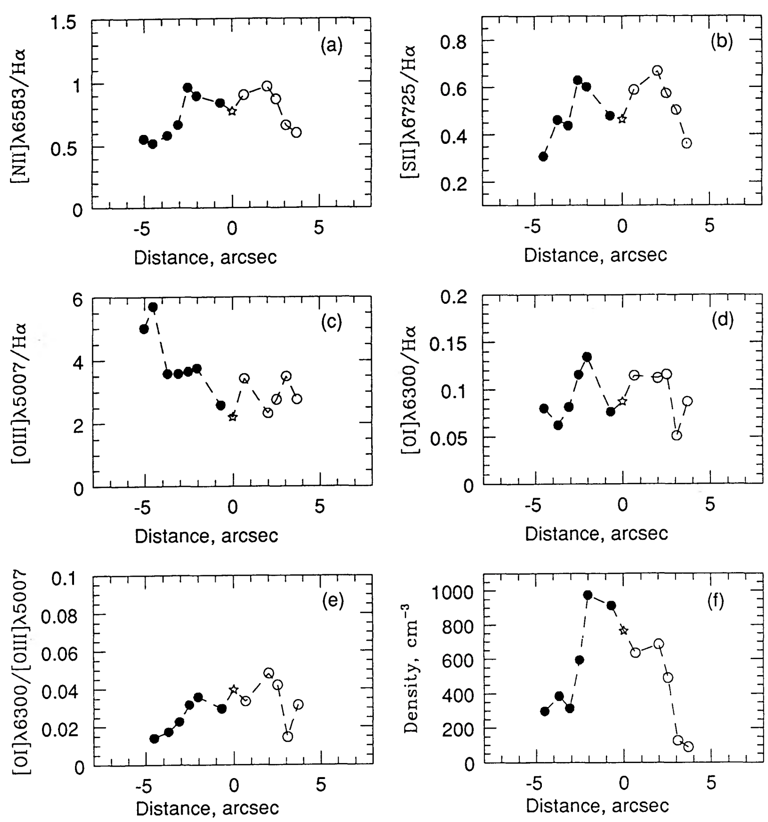

FIG. 5.—Line ratios plotted vs. axial distance from the nucleus along PA 125°. Open and filled circles have the same meaning as in Fig. 4.

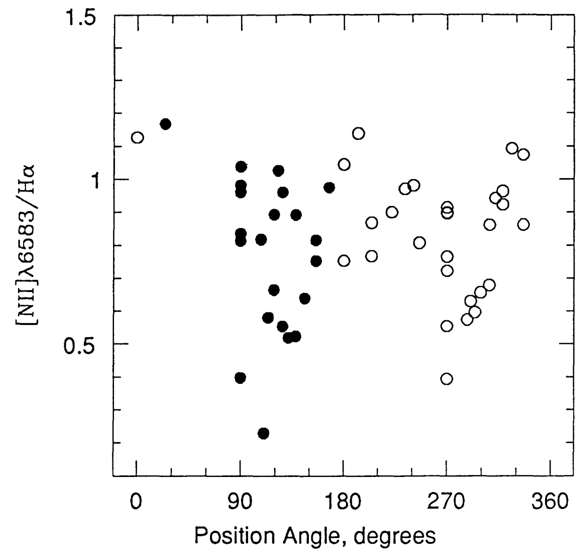

FIG. 6.—[N II] λ6583/Hα plotted vs. position angle. North is at 0°, east at 90°. Open and filled circles have the same meaning as in Fig. 4.

6. The [N II] λ6583/Hα angular dependence suggests that the ionizing flux is higher along the radio axis in PA 125°, although other effects may play an important role as well.

4. PHYSICAL CONDITIONS IN THE ENLR

In this section we use various line ratios to estimate the physical conditions, such as electron density and electron temperature, in the gas clouds in the extended emitting region. Observed line ratios, however, are affected by dust and need to be corrected for reddening before interpretation.

4.1. *Reddening*

The Galactic reddening is taken to be $E(B-V) = 0.03$ mag in the direction of Mrk 573 (Burstein & Heiles 1984). Reddening internal to the host galaxy is much more difficult to estimate. HWW91 studied the color maps of the nuclear region in Mrk 573 and found that localized features on the [O III] λ5007/(Hα + [N II]) map cannot be attributed simply to reddening. Our continuum images are not deep enough to extract reliable color gradient information for derivation of continuum reddening.

The most commonly used reddening indicator in the optical region is the ratio of the Balmer lines. In Seyfert galaxies the intrinsic Hα/Hβ ratio is believed to be 3.0–3.1, higher than the recombination case B value of 2.87, due to the much harder ionizing spectrum (Halpern & Steiner 1983; Gaskell & Ferland 1984). Recently, Binette et al. (1990) have argued that the intrinsic Balmer decrement could be as steep as 3.3–3.4 if dust is mixed in with the ionized gas. We measure Hα/H$\beta \approx 4.2$ at the position of the nucleus which is consistent with the ratio of 4.3 measured by Koski (1978) within a 2".7 × 4" slit. Both measurements, however, differ from the value of 2.9 measured by Kinney et al. (1991) using a much larger aperture of 15" × 15". This larger aperture could account for some of the difference based on the fact that reddening is much lower in the outer parts of the galaxy. Assuming an intrinsic Hα/Hβ = 3.0, we obtain $E(B-V) \approx 0.30$ at the position of the nucleus. The observed Hα/Hβ ratio increases from about 3 some 4" west of the nucleus to about 5 some 2"–2".5 on the east side and then drops further out. The lower reddening on the west side of the nucleus is consistent with the HWW91 color map.

The other methods of reddening estimation in the optical region include different combinations of the [O II] and [S II] line ratios (Allen 1979; Malkan 1983; Tsvetanov & Yancoulova 1989). In general, these require measuring much weaker lines, but the intrinsic ratios can be predicted reliably. The [S II] λ4069 line (the weakest one) is detected only at the position of the nucleus and neighboring pixels. All mentioned combinations give reddening of order of $E(B-V) \approx 0.35$ mag, consistent with the figure given in Malkan (1983) based on his measurements.

Our estimates compare with the value of $E(B-V) = 0.24$ mag derived by MacAlpine (1988) from the He II λ1640/λ4686 line ratio. Both UV and optical lines were measured through a large aperture intermediate in size between those used by Koski and Kinney et al. Nevertheless, relative line ratios were very close to those obtained by Koski. For the purposes of this study we shall assume $E(B-V) \approx 0.30$ mag within the inner most 3" diameter at the position of the nucleus and no reddening outside.

4.2. *Density and Temperature*

The electron density has been determined from the [S II] λ6716/λ6731 line ratio (see Osterbrock 1989). Figure 4*f* shows the density as a function of radial distance from the nucleus. Despite the relatively large individual errors a trend of density decreasing outward is clearly seen. In Figure 7 we present the same data averaged in 0".5 bins in an attempt to show the gradient more clearly. The density N_e drops from $\sim$800 cm^{-3} at the position of the nucleus and approaches the low density limit some 4" away.

The large error bars in Figure 7 do not allow us to determine the exact shape of the density radial dependence—the data are consistent with several different curves. If gas clouds are in equilibrium with an isothermal, hydrostatic atmosphere, their radial density profile may be modeled as $N(r) = N_0[1 + (r/r_0)^2]^{-3\beta/2}$, where r_0 is the core radius and β is the mass

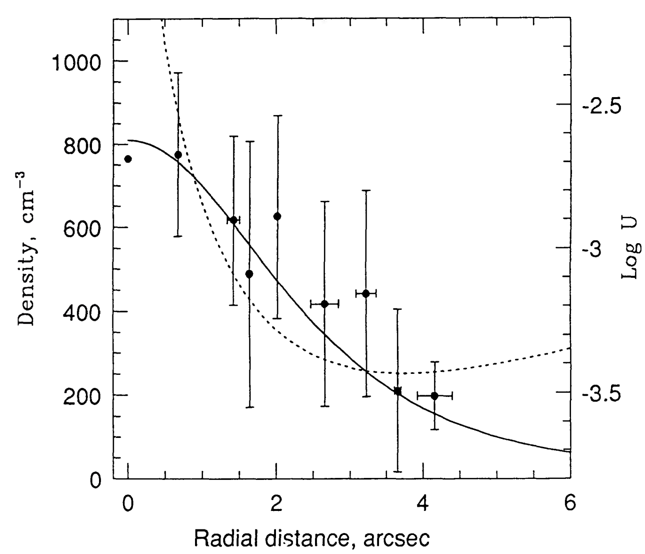

FIG. 7.—Density gradient along radial distance. Data points are averaged mean in 0".5 bins. Continuous curve shows an isothermal, hydrostatic density profile $N(r) = N_0[1 + (r/r_0)^2]^{-\beta/2}$ with $N_0 = 800$ cm^{-3}, $r_0 = 3".5$ and $\beta = 1.25$. The correspondent ionization parameter dependence is also shown (*dashes*). The right-hand scale is arbitrary.

deposition rate. For $\beta > \frac{2}{3}$ this type of density dependence has one important characteristic—the ionization parameter will first decrease with distance up to a certain radius and then increase further out (see Fig. 7). This is consistent with the positive excitation gradient found in IC 5063 by Colina, Sparks, & Macchetto (1991, hereafter CSM91). Robinson et al. (1987) find that extended emission-line regions around some radio galaxies often show a larger ionization parameter than the galaxy nucleus. In Mrk 573 we also find an outwardly increasing ionization parameter (see § 5.2.1 below).

The electron temperature can be calculated from the [O III] $\lambda(4959 + 5007)/\lambda 4363$ nebular to auroral line ratio, which is practically insensitive to density for $N_e \leq 10^4$ cm^{-3}. We have used a tabulation based on a five level atom code, which is essentially indistinguishable from the approximation given by Osterbrock (1989, p. 121).

The temperatures obtained in this way from our low-resolution spectra (PA 270°, through the nucleus) are in the range 13,000–17,000 K. The formal mean value is $T_e = 14{,}750 \pm 1650$ K (or $T_e = 14{,}160 \pm 665$ K if the most deviant point is excluded).

Another line ratio sensitive to T_e is [S III] $\lambda(9069 + 9532)/\lambda 6312$. The weakest of these three lines $\lambda 6312$ is seen in the wing of [O I] $\lambda 6300$ only within 1″ of the nucleus in our high-resolution spectra (see Fig. 8). Decomposition of this blend with Gaussian profiles suggests flux ratio of F([S III] $\lambda 6312$)/F([O I] $\lambda 6300$) ≈ 0.25. Using this ratio and measurements of $\lambda 9069$, $\lambda 9532$, and $\lambda 6300$ from the low-resolution spectra, we estimate $F(9069 + \lambda 9532)/F(\lambda 6312) \approx 40$, which corresponds to electron temperature $T_e \sim 14{,}000$ K, very similar to the value we get from the [O III] line ratio.

4.3. *Mass of the Emitting Gas*

Both the amount of the emitting gas and the filling factor can be estimated from the luminosity of the emission lines assuming the usual case B conditions (see Osterbrock 1989). The mass of the gas is given by

$$M_{\rm gas} = (N_p m_p + N_{\rm He} m_{\rm He})Vf \approx 1.4 N_p m_p L(\mathrm{H}_\alpha) j(\mathrm{H}_\alpha)^{-1} , \quad (1)$$

where $L(\mathrm{H}_\alpha)$ is the luminosity and $j(\mathrm{H}_\alpha)$ is the emissivity in Hα, V is the volume of the emission region, and f is the filling factor.

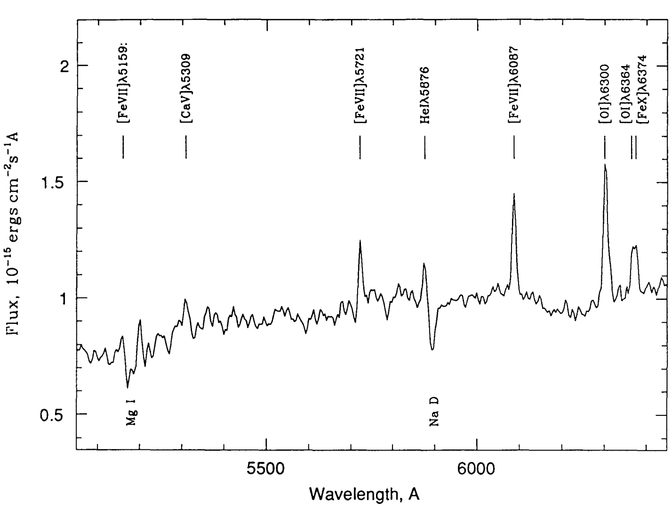

FIG. 8.—Part of the nuclear (2″ aperture) spectrum of Mrk 573 with high ionization lines.

A reasonable approximation is $N_{\rm He} = 0.1 N_p$, and $N_e = (N_p + 1.5 N_{\rm He})$. Assuming further that $T_e \approx 15{,}000$ K throughout the ENLR, the emissivity is $j(\mathrm{H}_\alpha) = 2.65 \times 10^{-25} N_p N_e$ ergs cm^{-3} s^{-1}. The flux in Hα is estimated from our narrow-band Hα + [N II] image. Spectroscopic data indicate that Hα contributes 40%–55% of the flux in that filter, which leads to log $F(\mathrm{H}_\alpha) = -12.33 \pm 0.1$ ergs cm^{-2} s^{-1} [the average ratio [N II] $\lambda 6583$/H$\alpha = 0.83 \pm 0.25$ and the uncertainty dominates the error in F(Hα)]. Our estimate is consistent to within 17% with the value of log $F(\mathrm{H}_\alpha) = -12.41$ ergs cm^{-2} s^{-1} measured by Kinney et al. (1991) through a 15″ × 15″ aperture. This gives $M_{\rm gas} \approx 3 \times 10^6\ M_\odot$, and a similar mass is determined if the [O III] $\lambda 5007$ line is used instead. This value should be considered as a lower limit since there is a strong density gradient outward. The amount of ionized gas is of the same order of magnitude as in the ENLR of IC 5063 (CSM91).

The gas in the ENLR is distributed unevenly and occupies only a small fraction of the volume. The filling factor is estimated from

$$f = L(\mathrm{H}_\alpha) j(\mathrm{H}_\alpha)^{-1} V^{-1} . \quad (2)$$

Assuming that the emitting region has a biconical shape, its volume is given by $V = 4/3\pi r^3(1 - \cos \beta/2)$, where β is the opening angle of the cone. We estimate $\beta = 80°$ (§ 5.1.2) and $r = 7\farcs5$ (5.5 kpc), which corresponds to $f \sim 8 \times 10^{-5}$. Again, this figure is of the same order of magnitude as in the case of IC 5063 (CSM91).

4.4. *High Ionization Stages*

Emission lines from highly ionized elements in the spectrum of Mrk 573 were first reported by Koski (1978). We register several lines from atoms in very high ionization stages, such as [Fe VII] $\lambda\lambda 5721$, 6087, [Fe X] $\lambda 6375$ and [Ca V] $\lambda 5309$, at the position of the nucleus and from the neighboring pixels within 1′–1″.5 on the SE side. Figure 8 shows a part of the nucleus spectrum of Mrk 573 with these lines. In principle, such high ionization stages of Fe [ionization potential $\chi(\mathrm{Fe}^{+6}) = 100$ eV, $\chi(\mathrm{Fe}^{+9}) = 235$ eV] can be achieved by either collisional ionization in a hot medium ($T_e \approx 10^6$ K) or by photoionization by a high-energy ($h\nu > 100$ eV) EUV/soft X-ray source. There are couple of arguments that the latter case applies in this object.

Nussbaumer & Storey (1982) have calculated [Fe VII] line ratios as a function of N_e and T_e. These are two lines ratios in the observed wavelength range that can be used as probes of the electron density and temperature. The line ratio $\lambda 5159/\lambda 6087$ is sensitive to density in the range $10^4 < N_e < 10^8$ cm^{-3}. Line measurements of Koski (1978) indicate a ratio [Fe VII] $\lambda 5159/\lambda 6087 \sim 0.2$. There is some indication that we see traces of [Fe VII] $\lambda 5159$. A comparison with the spectrum of a normal galaxy of the same Hubble type (Pickles 1985) shows that there is a small excess at the position of $\lambda 5159$ of order of 3 σ. If this is the case the ratio [Fe VII] $\lambda 5159/\lambda 6087 \sim 0.1$–0.2, which leads to $N_e \approx 10^6$–10^8 cm^{-3}. The [Fe VII] $\lambda 3759/\lambda 6087$ line ratio is almost insensitive to N_e and can be used to put a limit on the temperature. We do not detect [Fe VII] $\lambda 3759$ and estimate conservatively $\lambda 3759/\lambda 6087 < 0.25$. This rules out temperature higher than 60,000 K since in that case the ratio should have been above 1.0 in the expected density range.

4.5. *Photon Budget*

One way of checking whether the ionizing field is collimated is to compare the number of ionizing photons seen by the

ENLR gas with the number of ionizing photons emitted in the direction of Earth. The method is based on the assumption that the number of intercepted ionizing photons is proportional to the number of recombination photons. The hydrogen line flux, say $F(\mathrm{H}\alpha)$ or $F(\mathrm{H}\beta)$, is used to find the total number of Balmer recombination photons, observed at Earth, N_{rec} and N_{ion}, the total number of ionizing photons at Earth, is calculated from the observed UV spectrum assuming $F_\nu \propto \nu^{-\alpha}$:

$$\frac{N_{\mathrm{rec}}}{N_{\mathrm{ion}}} = \frac{\alpha_{\mathrm{B}}}{\alpha^{\mathrm{eff}}_{\mathrm{H}_\alpha}} \frac{\alpha F(\mathrm{H}_\alpha)}{\nu_{\mathrm{H}_\alpha} F_\nu(912\ \mathrm{Å})} \quad (3)$$

The ratio $N_{\mathrm{rec}}/N_{\mathrm{ion}}$ is a probe of the collimation hypothesis. In an isotropic case $N_{\mathrm{rec}}/N_{\mathrm{ion}} = C$, where $C = \Omega/4\pi$ is the covering factor, and hence $N_{\mathrm{rec}}/N_{\mathrm{ion}} > 1$ would be a strong indication that the ionizing field is anisotropic. It is important to note that ratio $N_{\mathrm{rec}}/N_{\mathrm{ion}}$ does not depend on the distance to the object.

Most recently, Kinney et al. (1991) have applied this method to 15 Seyfert 2 galaxies. For Mrk 573, in particular, they find $\alpha = 0.9 \pm 0.5$ from the *IUE* observations and estimate $N_{\mathrm{rec}}/N_{\mathrm{ion}} \approx 1$. In their estimate, however, they assume reddening $E(B-V) = 0$ mag and covering factor 1. Our measurements show that circumnuclear part of the ENLR emission is subject to some extinction. If we assume that flux from the inner 3″, which contains ~60% of the total emission in Hα + [N II], suffers a reddening of $E(B-V) = 0.30$ mag, then N_{rec} has to be increased by ~50%. In case of a biconical structure with an opening angle $\beta = 80°$ (see § 5.1.2), only 25% of the sky is illuminated. All these arguments lead to $N_{\mathrm{rec}}/N_{\mathrm{ion}} \geq 5$ and perhaps higher, since most probably not all ionizing photons in the direction of the ENLR are intercepted.

Similarly, we can estimate the $N_{\mathrm{rec}}/N_{\mathrm{ion}}$ ratio for photons with energy above $h\nu = 100$ eV from the observed [Fe VII] λ6087 luminosity. Assuming the same shape of the ionizing continuum, we have

$$\left(\frac{N_{\mathrm{rec}}}{N_{\mathrm{ion}}}\right)_{h\nu > 100\mathrm{eV}} = \frac{1}{n(^1D_2)h\nu A(\lambda 6087)} \frac{\alpha F(\lambda 6087)}{\nu F_\nu(100\mathrm{eV})}, \quad (4)$$

where $^1D_2$ is the relative population of the upper level of λ6087 as tabulated by Nussbaumer and Storey (1982). If electron temperature in the Fe^{+6} zone is similar to the temperature determined for the O^{+2} one, i.e., $T_e = 15{,}000$ K, and $N_e = 10^7$–10^{-8} cm^{-3} then $n(^1D_2) = (1.14$–$3.41) \times 10^{-2}$. We determine $F(\lambda 6087) = 1.02 \times 10^{-14}$ ergs cm^{-2} s^{-1} by summing flux in all pixels where [Fe VII] λ6087 is detected. The value is very close to Koski's measurement of 0.94×10^{-14} ergs cm^{-2} s^{-1}. Substituting these figures into equation (5), we obtain $(N_{\mathrm{rec}}/N_{\mathrm{ion}})_{h\nu > 100\ \mathrm{eV}} = 3$–$10$.

5. MODELING

The analysis presented in the previous section required relatively few common assumptions. For further understanding of the physical processes in the ENLR, however, it is necessary to model both the kinematics and excitation structure of the emitting gas. We try to model the velocity and the ionization pattern separately, although there might be some important interrelations especially close to the central source. The models presented here are rather general and aim only to put constraints on possible parameters.

5.1. *A Geometric and Velocity Model*

Following the initial discussion of the velocitty field of the ENLR in Mrk 573 (Tsvetanov 1989), we have tried to reproduce the observational features in § 3.4 by a biconical structure. The basic idea of the model is that of anisotropic ionizing radiation illuminating the ISM of the host galaxy. The gas in the ISM takes part in normal galaxy rotation, which is the main velocity component, but some radial motions may be present in addition. The brightness and velocity picture we observe is determined by the combination of several factors as illuminated matter distribution and orientation effects, etc. It is obvious that such a model has many free parameters, but some useful limits on the parameters can be established, and effects of varying many of them can be studied.

5.1.1. *Model Parameters*

The basic parameters needed to characterize the model are the opening angle of the bicone, its inclination to the rotation axis of the galaxy, the variation of velocity with radius, and the viewing angle with respect to the rotation axis. A filled biconical shape with opening angle β was created in a three-dimensional array with the symmetry axis of the bicone tilted at an angle θ to the y-axis. A rotation about the y-axis is applied either in the form of solid body rotation curve ($V_r = ar$) or as a rotation curve. The x, y, and z components of the velocity at each matter point are generated. The x, y, and z velocity components of radial expansion can also be generated. The combination of a rotating and expanding bicone is facilitated by summing the separate components of velocity. An emission versus radius relation is also applied to the basic form. The velocity and emission cubes can then be tilted to the desired orientation so that when collapsed along the x, y, or z axis the desired projection is produced. Fuller details of the model method are given in Walton, Walsh, & Sahu (1990). The variables which were not of direct interest in matching the model with the observational parameters (viz. temperature vs. radius, emission vs. radius, and turbulent velocity) were not varied in the modeling. In order to simulate the observed data, the peak velocity of the profile at each spatial pixel was found and written out to a two-dimensional array. This array can then be directly compared with Figure 3.

5.1.2. *Results of the Velocity Modeling*

The bioconical emission-line region must be viewed at some angle to its axis of symmetry to produce the elongated shape, but not larger than the bicone semi-opening angle (else a strongly bilobal form would result). The position angle of the long axis of the EELR and it projected zero velocity axis are the same to within ~5°, so the rotation axis is assumed to be contained in the plane of the axis of the ENLR and observer. A number of models were run to explore the effects of varying tilt of the structure to the rotation axis, bicone opening angle, and velocity structure. The following model is proposed which matches fairly well most of the observed behavior. A bicone of opening angle β of 80° is tilted by θ of 80° to the rotation axis and has a rotation curve with maximum value around 285 km s^{-1}. In order to match the large velocity extent of the observed structure, it proved necessary to tilt the bicone at such a large angle to the rotation axis (θ) so as to avoid having an excessively large rotation velocity. The bicone is viewed at an offset angle of 35° to its symmetry axis (i.e., within 5° to the edge of the cone). There is radial expansion of ~200 kms^{-1} at the center of the model, declining rapidly with distance from the nucleus. The whole structure is tilted at a position angle of 125°. Figure 9 (Plate 11) shows the color-coded velocity map and the adopted velocity model (blue = blueshifted; red = redshifted; velocity range 4800–5500 km s^{-1} and −200 to +200 km s^{-1}, respectively). The model emission declines as distance from the center of the model squared and produces a

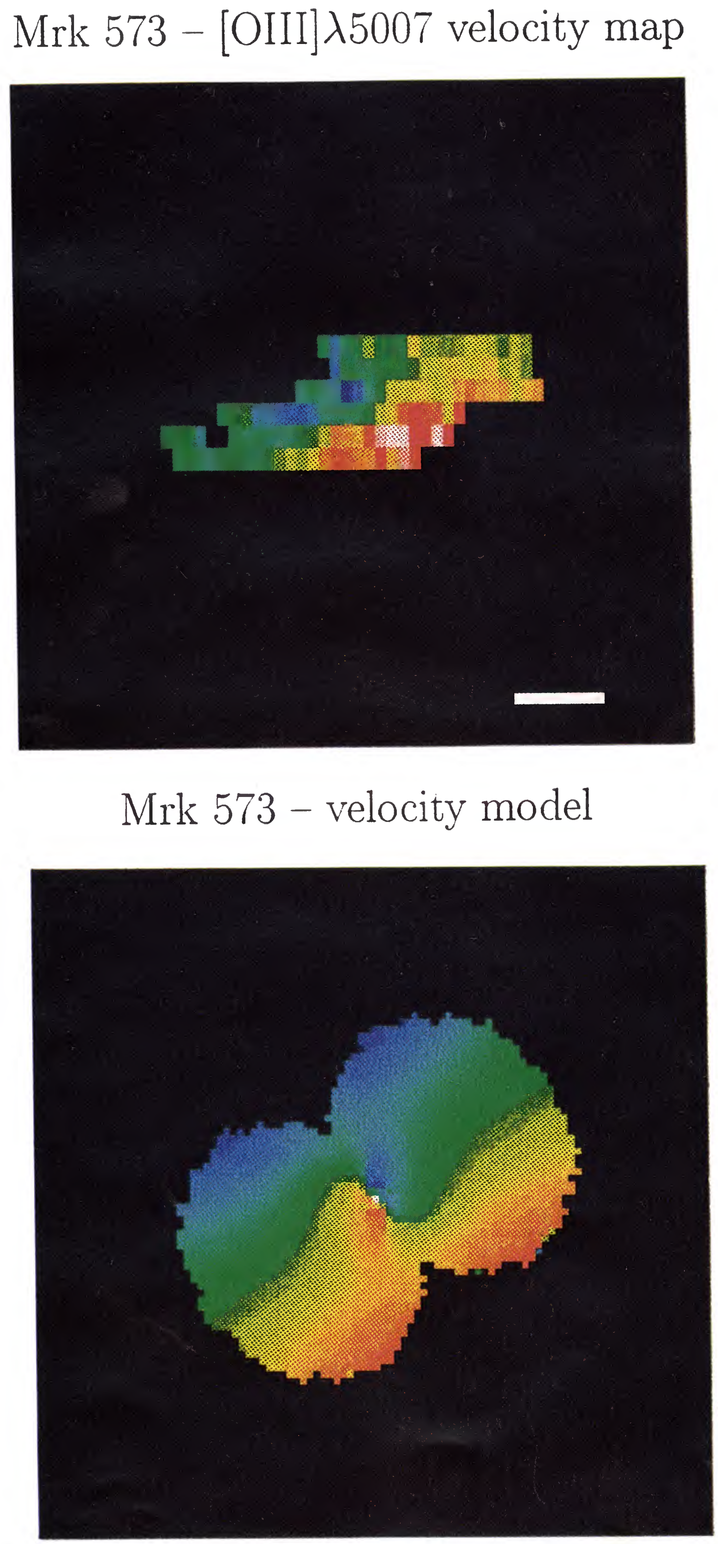

FIG. 9.—Color-coded velocity map and velocity model of the ENLR in Mrk 573. Blue = blueshifted, red = redshifted. Velocity range is 4800–5500 km s^{-1} and -200 to $+200$ km s^{-1}, respectively. The white bar in the upper panel corresponds to 5″.4.

TSVETANOV & WALSH (see 386, 493)

structure with an axial ratio of ~ 2. Figure 1*a* shows the projected flux map.

5.2. *Photoionization Model*

There are several indications suggesting that photoionization is the dominant excitation mechanism in the ENLR of Mrk 573. These are best seen on the line ratio diagnostic diagrams. Several different combinations of line ratios have been proposed to distinguish between different types of objects—H II regions, starburst, liners, AGNs (Baldwin, Phillips, & Terlevich 1981; Veilleux & Osterbrock 1987). We have adopted the combination suggested by Robinson et al. (1987), but with one difference—we use [O III] $\lambda 5007/H\alpha$ instead of [O III] $\lambda 5007/H\beta$ ratio since $H\beta$ is out of our wavelength range. The [O III] $\lambda 5007/H\alpha$ ratio is much more sensitive to the extinction, but general conclusions are most probably not affected since reddening is small in this object. Figure 10 presents line ratio diagrams based on our higher resolution data.

Observed line ratios throughout the ENLR of Mrk 573 are typical for Seyfert 2 galaxies or ENLRs (Veilleux & Osterbrock 1987; Robinson et al. 1987). They occupy the region characteristic of gas ionized by a hard nonthermal spectrum. This gives us confidence that the nucleus is the source of the ionizing flux. In order to understand further the physical conditions in the ENLR, we have compared the observed line ratios with photoionization models. We have used the multipurpose code MAPPINGS (cf. Binette, Robinson, & Courvoisier 1988 and references therein) which computes the line emissivities of a gas cloud exposed to an ionizing radiation. Given the geometry, the strength of the emission lines is governed by the shape of the ionizing spectrum F_ν, the density, and the ionization parameter U, which is defined as

$$U = \frac{Q_{\rm ion}}{4\pi r^2 c N_{\rm H}} \tag{5}$$

where $Q_{\rm ion}$ is the ionizing photon luminosity, r the distance to the cloud, $N_{\rm H}$ is the hydrogen number density, and c is the speed of light. We have considered three alternative ionizing continua—a power law ($F_\nu \propto \nu^{-\alpha}$), thin accretion disk (Pringle 1981), and a blackbody. For each of the input spectra, we have computed an ionization sequence of models with a constant density $N_{\rm H} = 100\ {\rm cm}^{-3}$ and a solar composition.

In our analysis of the observed data, we followed the procedure of Robinson et al. (1987), and all their main conclusions apply here as well. There are, however, several important differences. Although our data occupy a portion of the region populated in their diagrams, the spread of the points reflects real gradients in physical conditions of the ENLR in a single object and not in an ensemble of objects. Models with a single power-law input spectrum do not produce a good fit to the data. The other two incident spectra produce much better fit and are not very much different from one another. The blackbody temperature, however, needs to be very high ($T_{\rm BB} >$ 150,000 K), which effectively rules out an "early-type" origin

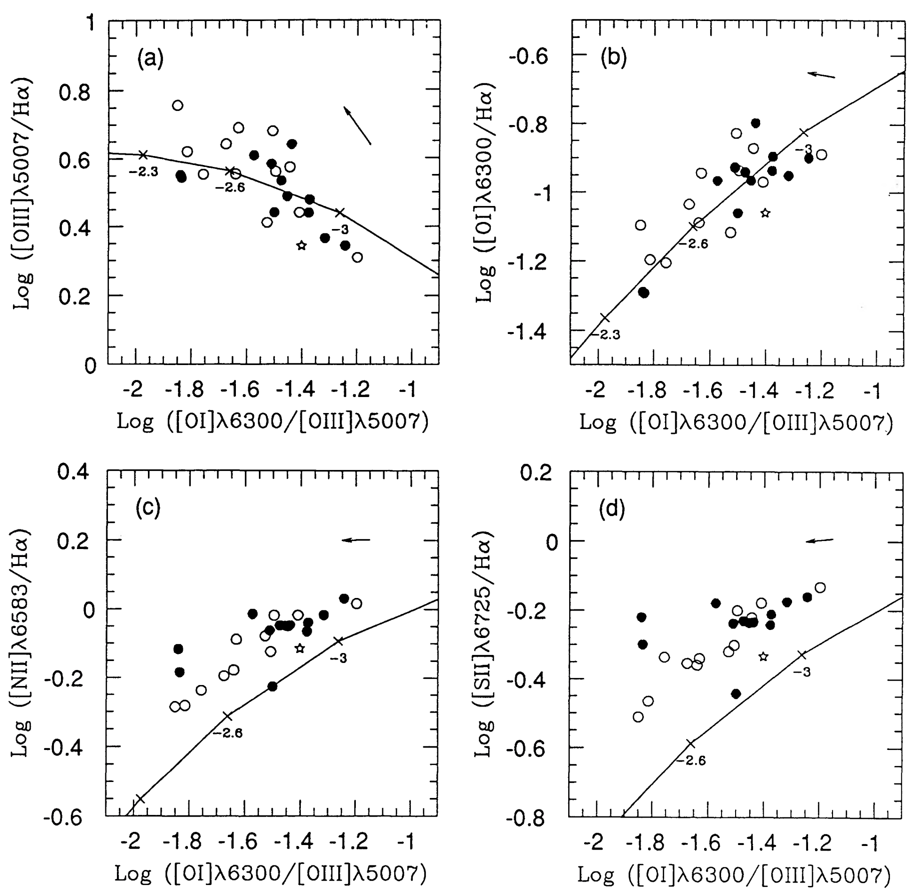

FIG. 10.—Line diagnostic diagrams. Open and filled circles have the same meaning as in Fig. 4. Continuous lines represent a constant density ($N = 100\ {\rm cm}^{-3}$) isobaric photoionization model with a thin accretion disk ionization spectrum of $T_{\rm char} = 400{,}000$ K (Pringle 1981). Crosses mark log $U = -3, -2.67, -2.33$. The arrow in each panel shows the effect of reddening correction. The length of the vector corresponds to $E(B-V) = 0.25$ mag.

of the ionizing source. A U sequence of models with an accretion disk input spectrum is presented in Figure 10. The low values of the [S II]/Hα ratio in the models may be a result of the poorly known dielectric recombination coefficient of S^{++} (L. Binette, private communication). Otherwise, the distribution of the data points in Figure 10 is naturally explained by excitation trends. The fact that we see basically a U sequence rules out any significant contribution to the ionization by young hot stars. Density gradients, though undoubtly present, may account for some of the spread of the points but cannot produce a fit alone.

5.2.1. *ENLR Excitation Structure*

As we discussed briefly in § 3.3, the line ratios [N II] λ6583/Hα, [S II] λ6725/Hα, [O I] λ6300/Hα and to lesser extent [O I] λ6300/[O III] λ5007 show similar behavior with distance, both radially and along the axis at PA 125° (see Figs. 4 and 5). In general, these ratios slightly increase up to approximately 2″ from the nucleus and then decrease farther out. In a pure photoionization picture, all these ratios are inversely proportional to the ionization parameter in the range $10^{-4} < U < 10^{-1}$. Obviously, the changes in Figures 4 and 5 are consistent with ionization parameter decreasing or being constant up to a certain distance from the nucleus and then increasing farther out. Figure 11 shows the radial dependence of the ionization parameter U as determined from our best fit to the line ratio diagnostic diagrams (Fig. 10).

It is important to note that similar behavior has been found in other objects as well. For instance, positive excitation gradients outward from the nucleus are detected in the ENLR of IC 5063 along different position angles (CSM91). Also, excitation conditions in the extended emission-line regions around powerful radio galaxies often require a larger ionization parameter than in the nucleus itself (Robinson et al. 1987).

In general, several different effects could account for such a behavior—differential extinction, local ionizing or heating sources, abundance gradients, density gradients. Differential extinction is ruled out as a plausible reason for explaining the excitation gradient on the basis of the reddening distribution (HWW91) as well as by the fact that neither the [N II] λ6583/Hα nor the [S II] λ6725/Hα line ratios are sensitive to reddening. Local ionizing sources distributed over the ENLR, such as increased population of young stars, could be excluded on the basis of the line ratio diagrams and color distribution. Indeed, all around the ENLR observed line ratios are typical of photoionization by a much harder spectrum than expected from hot stars. In addition, young stars are expected to show up on the continuum images and, better, on the color map (continuum ratio) and no such traces are observed (see also HWW91). The other two effects may contribute to the observed excitation gradient. As we discussed in § 4.2, the density distribution is well described by an exponential decrease, which naturally leads to an increasing ionizing parameter at larger distances, and we favor this interpretation. Unfortunately, large uncertainties prevent more quantitative analysis, for which both higher signal-to-noise ratio higher spatial resolution data are needed.

5.2.2. *Angular Dependence of the Ionizing Flux*

The method we have used to determine the number of ionizing photons in a given direction can be described as follows. For a given position x, y with respect to the nucleus, where we have measured [S II] and [N II] lines, we estimate the ionizing parameter U from the best fit to the line ratio diagrams (Fig. 10). Actually, one can estimate U separately from [N II] λ6583/Hα and [O I] λ6300/Hα ratios using the same best fit model. If at the same position we have a density measure from the [S II] doublet ratio, we can calculate the number of ionizing photons coming from the nucleus as seen from the gas cloud(s) at x, y.

Figure 12 presents a plot of the number of ionizing photons, $Q_{\rm ion}$, versus angle θ from the axis at PA 125°—the cone axis. There is a clear tendency of the ionizing photon luminosity being higher along the axis than in the perpendicular direction. Unfortunately, the accuracy and spatial resolution of the measurements do not allow us to estimate the emission "polar diagram" more precisely, but rather that it has a general triangular shape. This distribution has a FWHM ~ 80°, which compares well with the cone opening angle as determined from the analysis of the velocity pattern.

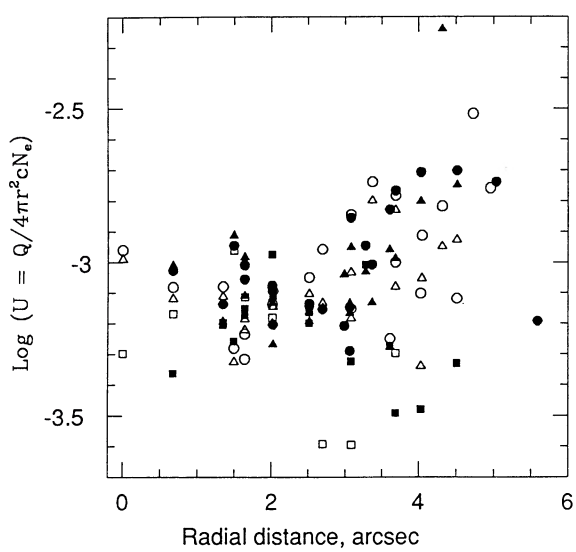

FIG. 11.—Ionization parameter vs. radial distance. Open and filled symbols have the same meaning as in Fig. 4. Circles, squares, and triangles correspond to U obtained through [N II] λ6583/Hα, [O I] λ6300/Hα, and [S II] λ6725/Hα line ratios, respectively.

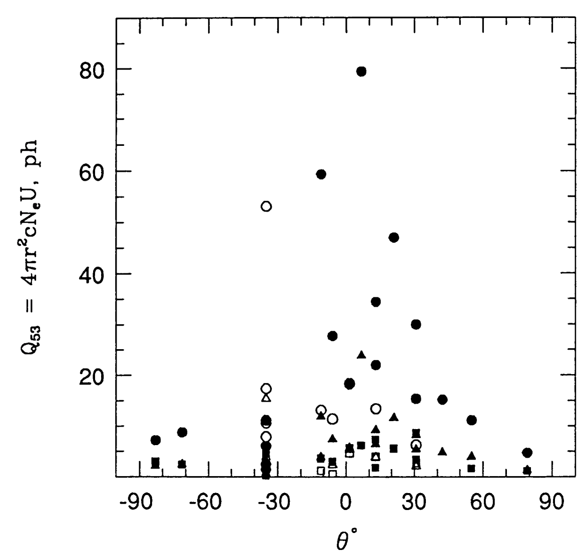

FIG. 12.—The number of ionizing photons vs. angle from the radio axis in PA 125°. All symbols have the same meaning as in Fig. 11.

6. DISCUSSION

Let us now turn to the "unified schemes" and see how results described in §§ 3–5 fit in with this general picture. The basic idea of the unification model, as applied to Seyfert galaxies, requires that in Type 1 objects the line of sight is within the opening angle of the cone, while type 2 objects are viewed from outside the cone. Therefore, many observational characteristics, such a broad lines, X-ray emission, etc., are all aspect-dependent. The overall morphology of the ENLR is obviously determined by projection effects as well as the gas distribution. In an ideal situation, when the line of sight is perpendicular to the cone axis and the gas is isotropically distributed, the ENLR would have a sharp biconical shape. Remarkably, the emission-line region in NGC 5252 appears quite close to this ideal situation (Tadhunter & Tsvetanov 1989). In a more general case, however, the appearance would be a rather elongated structure with axial ratio depending on cone opening angle, inclination of cone axis, and of course, gas distribution (see HWW88; Pogge 1989). The velocity pattern, on the other hand, would depend mainly on the combination of inclinations of the rotation axis with respect to both cone axis and line of sight.

It is quite clear that the picture emerging from both the observations and from the modeling fits in well in the unified scheme predictions. Both the morphology of the ENLR and the velocity map are explained in the framework of a biconical ionizing radiation illuminating the ISM of the host galaxy. The overall shape of the ENLR suggests that the line of sight is close to the edge, but within the cone opening angle. This seems to be in contradiction with the prediction that Seyfert 2's are viewed from outside the cone. This rough division, however, is most probably an oversimplification, and the transition is much smoother. There are many intermediate-type objects, such as Seyfert types 1.5, 1.8, 1.9, which show various spectral features reminicent of type 1's. Let us further assume as a working hypothesis a stratification picture (see Osterbrock 1989), in which the BLR is the most deeply hidden inside the obscuring formation (thick disk or torus), with the NLR, which is only partially obscured, farther out and on the largest scale the ENLR, which is basically unaffected by the central obscuring region. The high-ionization lines arise in an intermediate zone between the BLR and NLR, where both density and ionizing flux are high. It is then natural to expect to see coronal emission lines before broad line wings as the line of sight is moved progressively into the cone.

Another prediction of the unified theory is that the number of ionizing photons in the line of sight will be greatly reduced when looking outside of the cone opening angle. Indeed, Kinney et al. (1991) found such an energy deficit in many Seyfert type 2 objects. Our analysis of the photon budget in § 4.5 suggests that Mrk 573 does not have a very large deficit ($N_{\rm rec}/N_{\rm ion} \geq 1$). This, however, is generally consistent with our geometric model where the biconical emission line region is viewed at an angle only slightly smaller than the bicone semi-opening angle to produce in projection the observed elongated shape.

7. CONCLUSIONS

The results obtained from both narrow-band imaging and long-slit spectroscopy of the ENLR in Mrk 573, along with a possible explanation in the framework of the unified model, can be summarized as follows:

1. Images of Mrk 573 in [O III] λ5007, Hα + [N II] and [S II] $\lambda\lambda$6716, 6731 show an elongated emission line region of roughly $10'' \times 15''$ oriented at PA 125°. This is also the position angle of the projected radio axis. The morphology of the ENLR could be understood as a wide angle bicone structure viewed from within the cone opening angle, but close to the edge.

2. The excitation/reddening map, line ratio $\mathscr{R}$ = [O III] λ5007/(Hα + [N II]), shows an arclike maximum shifted at $\sim 4''$ toward the SE along the radio axis. A wide valley of reduced $\mathscr{R}$ crosses the nucleus roughly perpendicular to the main elongation axis. This could be interpreted as a shadow of the obscuring formation (torus?).

3. Physical conditions in the ENLR are in the expected range for a photoionized gas and are typical in comparison with other objects. The density of the emitting gas decreases outward from about 800 cm^{-3} at the nucleus and approaches the low-density limit some $4''$–$5''$ away. Reddening is modest at the position of the nucleus—$E(B-V) \approx 0.30$ mag—and quickly drops outside. The electron temperature is of the order of 15,000 K.

4. High-ionization emission lines, such as [Fe VII] and [Fe X], are detected at the position of the nucleus and in its immediate vicinity on the SE side. In the framework of the unified model, this is interpreted as a projection effect—the line of sight is within the cone but close to the edge, so we see only the intermediate zone where coronal emission lines arise.

5. There are two important features seen in the velocity map—the projected rotation axis is aligned to within the errors with the radio axes, and at the position of the nucleus the emission lines are blueshifted by more than 100 km s^{-1}. A possible interpretation is a wide-angle bicone ionizing field illuminating the ISM in the host galaxy. The gas takes part in a normal galaxy rotation and also has radial motions at least near the nucleus. The bicone structure is significantly tilted with respect to the rotation axis, but both axes appear in the same position angle due to projection effect.

6. The emission line spectrum all around the ENLR is well described by a photoionization from the nucleus. The ionization parameter U varies from 10^{-3} to almost 10^{-2}. There is a positive excitation gradient with distance from the nucleus. This is best explained by a density gradient—possibly a density profile in an isotropic atmosphere—where density drops outward faster than r^{-2} at larger radii.

7. Both the photon budget and the angular dependence of the ionizing field suggest higher density of the ionizing flux along the cone axis than perpendicular to it. The FWHM of the angular distribution is similar to that obtained from the velocity model, but higher signal-to-noise ratio data are necessary to put tighter constraints on the angular dependence of the ionizing field.

It is a pleasure to thank R. Fosbury, C. Tadhunter, and E. Meurs for many useful discussions stimulating this work. Z. T. is particulary grateful to L. Binette for providing access to the multipurpose code MAPPINGS as well as for the training in its use. We would like to thank Professor. A. S. Wilson for a careful reading of the manuscript and for a number of valuable comments and suggestions. This research was supported in part by NSF grant AST-8719207 and NASA NAG5-1079 to the University of Maryland and by the European Southern Observatory.

REFERENCES

Allen, D. A. 1979, MNRAS, 186, 1P
Antonucci, R. R. J., & Miller, J. S. 1985, ApJ, 297, 621
Baldwin, J. A., Phillips, M. M., & Terlevich, R. 1981, PASP, 93, 5
Barthel, P. D. 1989, ApJ, 336, 606
Binette, L., Calvert, N., Cantó, J., & Raga, A. C. 1990, PASP, 102, 723
Binette, L., Robinson, A., & Courvoisier, T. J.-L. 1988, A&A, 194, 65
Browne, I. W. A. 1989, in ESO Workshop Extranuclear Activity in Galaxies, ed. E. J. A. Meurs & R. A. E. Fosbury (Garching: ESO), 379
Burstein, D., & Heiles, C. 1984, ApJS, 54, 33
Colina, L., Sparks, W. B., & Macchetto, F. D. 1991, ApJ, 370, 102 (CSM91)
di Serego Alighieri, S. 1987, ESO Messenger, 48, 10
———. 1990, in Acquisition, Processing and Archiving of Astronomical Images, ed. G. Longo & G. Sedmak (Naples: OAC-FORMEZ) 311
Fosbury, R. A. E. 1989, in ESO Workshop Extranuclear Activity in Galaxies, ed. E. J. A. Meurs & R. A. E. Fosbury (Garching: ESO), p. 169
Gaskell, C. M., & Ferland, G. P. 1984, PASP, 96, 393
Halpern, J. P., & Steiner, J. E. 1983, ApJ, 269, L37
Haniff, C. A., Wilson, A. S., & Ward, M. J. 1988, ApJ, 334, 104 (HWW88)
———. 1991, ApJ, 368, 168 (HWW91)
Kinney, A. L., Antonnucci, R. R. J., Ward, M. J., Wilson, A. S., & Whittle, M. 1991, ApJ, 377, 100
Koski, A. T. 1978, ApJ, 223, 56
Lawrence, A. 1987, PASP, 99, 309
Lawrence, A., & Elvis, M. 1982, ApJ, 256, 410
MacAlpine, G. M. 1988, PASP, 100, 65
Malkan, M. A. 1983, ApJ, 264, L1
Melnick, J., Dekker, H., & D'Odorico, S. 1989, "EFOSC," ESO Operating Manual No, 4, Version 2
Miller, J. S., & Goodrich, R. W. 1990, ApJ, 355, 456
Nussbaumer, H., & Storey, P. J. 1982, A&A, 113, 21
Orr, M. J. L., & Browne, I. W. A. 1982, MNRAS, 200, 1067
Osterbrock, D. E. 1989, in Astrophysics of Gaseous Nebulae and Active Galactic Nuclei (Mill Valley: University Science Books)
Pickles, A. J. 1985, ApJS, 59, 33
Pogge, R. 1989, ApJ, 345, 730
Pringle J. E. 1981, ARA&A, 19, 137
Robinson, A., Binette, L., Fosbury, R. A. E., & Tadhunter, C. N. 1987, MNRAS, 227, 97
Tadhunter, C., & Tsvetanov, Z. 1989, Nature, 341, 422
Tsvetanov, Z. 1989, in Extranuclear Activity in Galaxies, ed. E. J. A. Meurs & R. A. E. Fosbury (Garching: ESO), 251
Tsvetanov, Z., Tadhunter, C., Peréz, E., & González-Delgado, R. 1989, in Extranuclear Activity in Galaxies, ed. E. J. A. Meurs & R. A. E. Fosbury (Garching: ESO), 19
Tsvetanov, Z. I., & Yancoulova, I. M. 1989, MNRAS, 707
Ulvestad, J. S., & Wilson, A. S. 1984, ApJ, 285, 439
Unger, S. W., Pedlar, A., Axon, D. J., Whittle, M., Meurs, E. J. A., & Ward, M. J. 1987, MNRAS, 228, 671
Urry, C. M., Maraschi, L., & Phinney, E. S. 1991, Comm. Ap., in press
Veilleux, S., & Osterbrock, D. E. 1987, ApJ, 63, 295
Walton, N. A., Walsh, J. R., & Sahu, K. C. 1990, A&A, 230, 445
Whittle, M., Pedlar, A., Meurs, E. J. A., Unger, S. W., Axon, D. J. A., & Ward, M. J. 1988, ApJ, 326, 125
Wilson, A. S., & Heckman, T. M. 1985, in Astrophysics of AGN and QSO, ed. J. S. Miller (Mill Valley: University Science Books), 39
Wilson, A. S., Ward, M. J., & Haniff, C. A. 1988, ApJ, 334, 121
Wilson, A. S., Xuening, W., Heckman, T. M., Baldwin, J. A., & Balick, B. 1989, ApJ, 339, 729
Yee, H. K. C., & Oke, J. B. 1978, ApJ, 226, 753